RESEARCH ARTICLE

PROGRESS IN PHOTOVOLTAICS WILEY

Upscaling of perovskite solar modules: The synergy of fully evaporated layer fabrication and all-laser-scribed interconnections

David B. Ritzer[1] | Tobias Abzieher[2] | Agit Basibüyük[1] | Thomas Feeney[2] | Felix Laufer[2] | Simon Ternes[1] | Bryce S. Richards[1,2] | Stefan Bergfeld[3,4] | Ulrich W. Paetzold[1,2]

[1]Institute of Microstructure Technology, Karlsruhe Institute of Technology, Eggenstein-Leopoldshafen, Germany

[2]Light Technology Institute, Karlsruhe Institute of Technology, Karlsruhe, Germany

[3]Research and Development, Bergfeld Lasertech GmbH, Aachen, Germany

[4]Laboratories for Laser Technology and Material Science, FH Aachen, Jülich, Germany

Correspondence
David B. Ritzer and Ulrich W. Paetzold, Institute of Microstructure Technology, Karlsruhe Institute of Technology, 76344 Eggenstein-Leopoldshafen, Germany.
Email: david.ritzer@kit.edu; ulrich.paetzold@kit.edu

Tobias Abzieher, Light Technology Institute, Karlsruhe Institute of Technology, 76131 Karlsruhe, Germany.
Email: tobias.abzieher@nrel.gov

Present address
Tobias Abzieher, National Renewable Energy Laboratory, Golden, CO, USA

Abstract

Given the outstanding progress in research over the past decade, perovskite photovoltaics (PV) is about to step up from laboratory prototypes to commercial products. For this to happen, realizing scalable processes to allow the technology to transition from solar cells to modules is pivotal. This work presents all-evaporated perovskite PV modules with all thin films coated by established vacuum deposition processes. A common 532-nm nanosecond laser source is employed to realize all three interconnection lines of the solar modules. The resulting module interconnections exhibit low series resistance and a small total lateral extension down to 160 μm. In comparison with interconnection fabrication approaches utilizing multiple scribing tools, the process complexity is reduced while the obtained geometrical fill factor of 96% is comparable with established inorganic thin-film PV technologies. The all-evaporated perovskite minimodules demonstrate power conversion efficiencies of 18.0% and 16.6% on aperture areas of 4 and 51 cm^2, respectively. Most importantly, the all-evaporated minimodules exhibit only minimal upscaling losses as low as 3.1%$_{rel}$ per decade of upscaled area, at the same time being the most efficient perovskite PV minimodules based on an all-evaporated layer stack sequence.

KEYWORDS
laser scribing, perovskite solar cells, solar modules, thermal co-evaporation, upscaling

---

D. B. Ritzer and T. Abzieher contributed equally to this work.

1 | INTRODUCTION

Hybrid metal-halide perovskite semiconductors are considered as one of the most promising candidates in the field of emerging photovoltaics (PV). As a result of their excellent optoelectronic properties[1–3] and an extensive research effort over the past decade, power conversion efficiencies (PCEs) of perovskite solar cells now exceed 25%.[4] Thus, from a performance point of view, perovskite solar cells are ready to compete with more well-established PV technologies such as wafer-based crystalline silicon, as well as thin-film based copper indium gallium diselenide (CIGS) and cadmium telluride (CdTe) technologies.[5] However, in view of the commercialization of perovskite PV, several key challenges remain unsolved including long-term operational stability, toxicity, and upscaling to industrially relevant device areas.[6–8] Extensive research on the composition of the perovskite absorber material and device architecture aims to increase long-term stability and reduce the reliance on harmful solvents and lead-containing precursors.[9,10] Scaling the technology requires processes that provide high homogeneity, reproducibility, and production yield independent of device area, ultimately enabling a process transfer from laboratories to commercial fabrication lines.[6,11]

Today, spin coating remains the most common laboratory-based method to deposit small-scale perovskite solar cells as it allows for simple screening of both materials and processes.[12–14] However, the transfer of developed spin-coating processes to larger areas is limited as process conditions are significantly changing for different substrate areas, requiring a meticulous reoptimization of process parameters and substitution of some fabrication steps (such as solvent quenching approaches).[15–17] As an alternative, scalable solution-based deposition techniques such as blade coating, slot-die coating, or inkjet printing have demonstrated scalability of perovskite PV to areas up to 804 cm[2].[15,18] (In order to ensure the comparability of presented results, all areas and PCE values are given in the following in relation to aperture area. To provide transparency, the originally reported

active area values are given in Table S1. The used area terminology for this work is defined in Figure S2.) For example, Deng et al. demonstrated a highly efficient and stable 29.5-cm[2] minimodule with a stabilized PCE of 18.6% (calculated from reported 20.2% active area PCE), utilizing blade coating and an improved defect compensation.[19] Regarding further upscaling, Di Giacomo et al. fabricated a 144-cm[2] perovskite PV module via slot-die coating, employing an optimized drying process enabling a stabilized PCE of 13.8% (calculated from reported 14.5% active area PCE).[20] Furthermore, the Panasonic Corporation demonstrated an 804-cm[2] perovskite PV module exhibiting an averaged initial PCE of 17.9%.[5] Despite these advances, upscaling perovskite solar cells via solution-based deposition techniques remains challenging, as apparent in the significant decline in performance when increasing the device area. This aspect is illustrated in Figure 1 that shows the PCEs as a function of aperture area for laboratory-scale solar cells and modules processed by different deposition techniques (further information is summarized in Figure S1 and Table S1).[5,16,17,19–87] In particular, blade coating—currently one of the most promising upscaling deposition techniques for perovskite PV—exhibits a PCE loss of 19.7%$_{rel}$, when increasing the device area from 0.8 to 42.9 cm[2].[43] Comparing the latest efficiency records of perovskite solar cells and modules processed by any technology, upscaling losses of 7.4%$_{rel}$ per decade (dec) of upscaled area are observed (see Equation S1).[5]

Minimizing the upscaling losses of perovskite PV requires addressing two criteria: (1) homogenous and defect-free deposition of all functional layers and (2) fabrication of module interconnections with optimal electrical properties and minimal lateral extension.[6] Despite all promises of solution-based deposition methods—such as high-throughput fabrication via roll-to-roll approaches—the inherent process properties pose significant challenges regarding the first criterion.[73,88] In particular, the interaction of solvents, solids, and the environment remains a problem as drying, nucleation, and crystallization in solution-based methods is complex to monitor with increasing
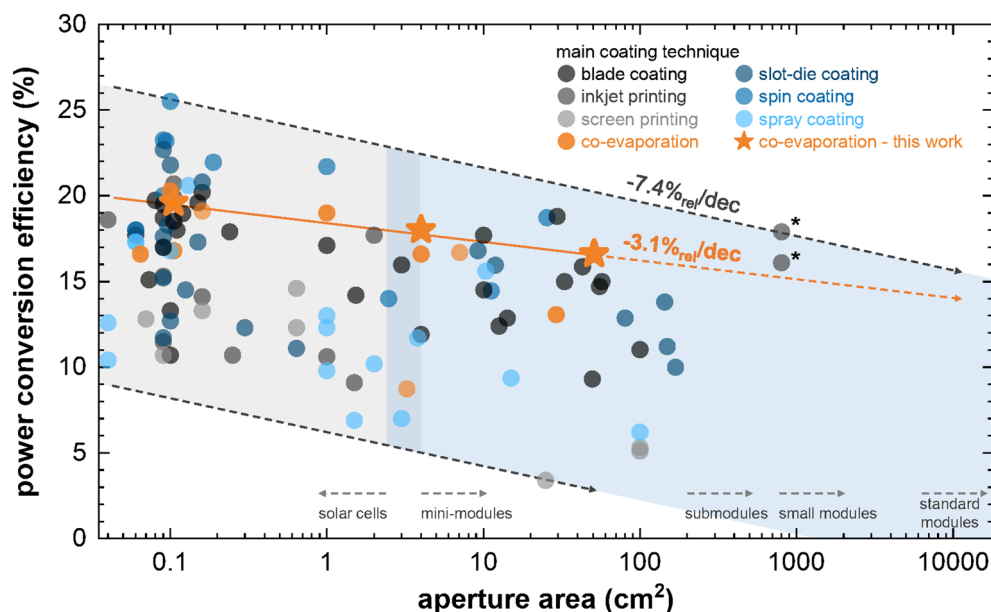

FIGURE 1 Power conversion efficiencies (aperture area values) as a function of the aperture area obtained for perovskite solar cells and modules processed with different scalable deposition techniques. Data points marked with an asterisk (*) represent recent solar module records from industry. Upscaling losses from recent record solar cells (typically 0.1 cm[2]) to record modules (804 cm[2]) are found to be 7.4%$_{rel}$/dec. Detailed information about the data points is summarized in the supporting information (see Figure S1 and Table S1). Data points of this work are highlighted with a star [Colour figure can be viewed at wileyonlinelibrary.com]

area.[89] The use of additives and the modification of the drying and crystallization dynamics via gas and solvent quenching have reportedly improved the homogeneity for larger areas of several square centimeters up to occasionally above 100 cm^2.[20,43,89–91] However, these adaptions further increase process complexity and complicate subsequent optimizations and upscaling in general.[92]

As an alternative to solution-based approaches, co-evaporation of organic and inorganic salts has been developed and proved to yield excellent homogeneity for areas up to 21 cm^2.[2,25,67,93,94] Today, vapor-based deposition techniques are the dominant technology for the vast majority of commercialized optoelectronic devices and in particular thin-film PV technologies. The focus on vapor-based methods in industry is founded on good homogeneity in material composition and layer thickness as well as high production yield.[95] Remarkable progress has been demonstrated with vapor-deposited perovskite solar cells achieving PCEs as high as 20.6%.[96] Recently, alternative absorber compositions—beyond the classical methylammonium lead triiodide (CH$_3$NH$_3$PbI$_3$) absorbers—were also introduced for vapor-based methods. These include multication perovskites,[97] which are known to provide better stability and performance,[98] wide-bandgap absorbers for the future use in tandem solar cells,[99] and lead-free perovskites.[100] Perhaps of particular interest is also the concept of fully vapor-based perovskite solar cells, as it reduces complexity and types of systems required. Despite the potential of vapor-based deposition techniques, there are currently few reports relating to vapor-based perovskite PV modules. First, a team composed of some of the present authors employed an all-evaporated layer stack to achieve 8.8% PCE in backward current–density–voltage (J–V) scan direction for a 3.2-cm^2 module (calculated from reported 12.4% active area PCE), while second, Li et al. demonstrated a 29.2-cm^2 aperture area device with a PCE of 13.1% (calculated from reported 18.1% active area PCE).[25,67]

Beyond challenges arising from the upscaling of the deposition process itself, thin-film PV modules require monolithic interconnection of solar cell stripes to compensate for the limited conductivity of the front transparent conductive oxide (TCO). As a consequence of the solar module interconnection, two loss mechanisms arise, namely, (1) contact resistance at the interconnections and (2) a reduction of the active area required for the interconnection.[101,102] Therefore, in order to maximize performance in thin-film PV modules, it is crucial to minimize these individual losses by employing suitable scribing methods and interconnection layouts. Realization of the three essential interconnection lines (commonly referred to as P1, P2, and P3) is performed via either mechanical scribing,[103] chemical etching, lift-off processes,[27,104] laser scribing,[59] or a combination of these methods. Mechanical scribing is a simple, cheap, and established process in the CIGS PV industry, relying on this method for the P2 and P3 scribing lines as laser scribing approaches commonly result in heat-induced shunts.[105,106] However, mechanical scribing is accompanied by unfavorable process restrictions such as tool wear, chip formation, and incompatibility with flexible substrates.[59,107]

All-laser-scribed thin-film solar module interconnection is an industrial standard and applied already for decades in amorphous silicon (a-Si), CdTe, and tandem thin-film a-Si-based modules.[108,109] The

process provides high throughput due to fast scanning speeds, low maintenance, and is compatible with flexible substrates due to non-contact processing.[43,110] Consequently, laser scribing is of key interest for perovskite solar module interconnections, enabling the fabrication of scribing lines of only few tens of micrometers lateral extension and of good electrical properties.[103,111] In this context, Di Giacomo et al. have demonstrated that resistive losses for an upscaling process of over two orders of magnitude in area can be limited to only about 3%$_{rel}$ by employing all-laser-scribed interconnection lines.[59] Furthermore, by developing a laser-scribed point contact interconnection scheme, Rakocevic et al. have shown that the active area loss can be reduced to as little as 1%$_{rel}$ for a 4-cm^2 aperture area device.[102]

It should be noted that most previous studies on all-laser-scribed interconnections of perovskite minimodules used more than one lasing source to process all three interconnection lines (e.g., with different wavelengths) and in many cases picosecond and femtosecond laser sources were applied.[59,69,112–114] While shorter pulses commonly allow for more selective laser ablation, the complexity and also price of such lasing sources increases below 100 picoseconds. For this reason, production sites of established thin-film PV technologies (e.g., a-Si and CdTe) make use of nanosecond lasing sources.[115,116] However, a few studies also report on the exclusive use of nanosecond lasers for fabrication of perovskite solar module interconnections. Ren et al. have demonstrated the feasibility of utilizing a single 532-nm nanosecond laser source to fabricate all three interconnections lines for a spin-coated layer stack, reporting a promising 18.7% PCE for a 25-cm^2 (aperture area) perovskite minimodule with 90.8% geometrical fill factor (GFF) and reference solar cells of 22% PCE.[70] Furthermore, employing a 1064-nm nanosecond laser source and a co-evaporated perovskite layer with solution-processed transport layers, Li et al. successfully fabricated an all-laser-scribed 7.1-cm^2 (aperture area) perovskite minimodule with 90.7% GFF and 16.7% PCE (calculated from reported 18.4% active area PCE), reference solar cells exhibiting 19.1% PCE.[24] Nevertheless, upscaling losses of 14.8%$_{rel}$ (Ren et al.) and 12.6%$_{rel}$ (Li et al.) exhibit a substantial deficit to the theoretically obtainable losses. Consequently, an optimization of GFF and of resistive losses is required. It is further reasonable to assume that a transfer to vapor-based deposition can reduce losses induced by process parameter changes occurring when scaling up deposition area of spin coating.

In response to these challenges, this work combines for the first time the concept of all-evaporated perovskite solar modules with all-laser-scribed monolithic interconnections, mitigating upscaling losses to values achieved for state-of-the-art PV technologies such as CIGS, crystalline silicon (c-Si), and CdTe. By utilizing vapor-based deposition and a nanosecond laser for scribing of interconnections, both being established manufacturing methods for other thin-film technologies, facile upscaling of device area for perovskite PV is demonstrated. First, detailed analyses of the scribing process by scanning electron microscopy (SEM), energy-dispersive X-ray (EDX) analysis, and measurements of characteristic resistances, which affect series and parallel resistances of finished devices, are presented. Employing a 532-nm nanosecond laser and adjusting only its fluence and scribing speed, all three scribing lines exhibit selective material removal. The obtained

GFF reaches up to 96% and the scribing speed at 10-kHz repetition rate corresponds to 50, 33, and 100 mm s^{-1} for the P1, P2, and P3 scribing line, respectively. Making use of photoluminescence (PL) imaging and laser beam-induced current (LBIC) mapping, the homogeneous layer deposition of the all-evaporated perovskite layer stack sequence is validated. Efficient PV minimodules with PCEs of 18.0% and 16.6% on aperture areas of 4 and 51 cm^2, respectively are demonstrated. Considering the increase in device area by a factor of up to 500, upscaling losses as small as 3.1%$_{rel}$/dec of upscaled device area are obtained.

2 | RESULTS AND DISCUSSION

2.1 | Facile all-laser-scribed interconnection processing

Perovskite PV needs strategies that offer simple, industrially applicable, yet highly efficient upscaling in order to reach industrial maturity. To address this challenge, the combination of an all-laser-scribed interconnection process and all-evaporated layer stack sequence is demonstrated in this work. Figure 2 illustrates a potential future industrial inline process for the fabrication of perovskite solar modules, combining vapor-based deposition of all functional layers and laser scribing of the module interconnection lines. In the following, laser scribing of all three module interconnection lines by employing a 532-nm nanosecond laser setup is shown to be a simple approach combining the fundamental requirements of (1) high scribing quality, (2) facile process optimization and controllability, and (3) good integrability into a deposition system. Optimization is performed based on the all-evaporated layer stack sequence of indium tin oxide (ITO), 2,2′,7,7′-tetra(N,N-di-p-tolyl)amino-9,9-spirobifluorene (spiro-TTB), methylammonium lead iodide ($CH_3NH_3PbI_3$), fullerene (C_{60}), bathocuproine (BCP), and gold (Au) or silver (Ag) that has recently been reported for perovskite solar cells of 0.105-cm^2 active area (see inset in Figure 2).[117] Utilizing the exact same evaporation system, materials,

and parameters for deposition ensures applicability of previously presented chemical analyses and allows focusing in this work on characterization methods suited to evaluate the properties and quality of upscaled layers. The custom-built laser scribing setup consists of an enclosed optical system mounted underneath a glovebox and a sample compartment inside the glovebox, enabling easy accessibility for maintenance, while minimizing health risks posed by the laser and the sample's chemical constituents. Combining multiple standard components, the optical system integrates a conventional 1064-nm nanosecond neodymium-doped yttrium orthovanadate (Nd:YVO$_4$) laser with frequency doubling, a compact galvanometer scanner system for fast and flexible laser beam deflection with accurate focusing, and a camera system for high precision alignment during the multiple monolithic scribing steps. The sample compartment is separated from the optical system by an optical window enabling possible integration into a future inline deposition process, while the nitrogen atmosphere inside the glovebox protects functional layers of the solar module against detrimental effects of water, oxygen, or dust particles. During laser scribing, samples inside the glovebox are under permanent laminar nitrogen flow to remove ablation debris from the surface. In order to reduce process complexity, the laser is operated at one ablation wavelength (here 532 nm), continuous repetition rate (here 10 kHz), and at one focus length for all three ablation processes. The three individual scribing lines of the solar module are optimized with regard to characteristic resistances, resulting in high-quality laser scribing lines with well-defined and well-separated process windows. Scribing layouts and contacting schemes are depicted in Figure S3.

In order to illustrate the ease of optimizing the two-parameter scribing process, the influence of fluence on the characteristic resistance is discussed. The P1 and P3 scribing lines separate individual solar cell stripes from each other by insulating adjacent front electrode and back electrode stripes, respectively (i.e., infinite series resistance over these scribing lines). The P2 scribing line connects two neighboring cell stripes by establishing a contact between the rear electrode and the front TCO. A serially interconnected solar cell is depicted in the inset of Figure 2. Targeting a minimized detrimental
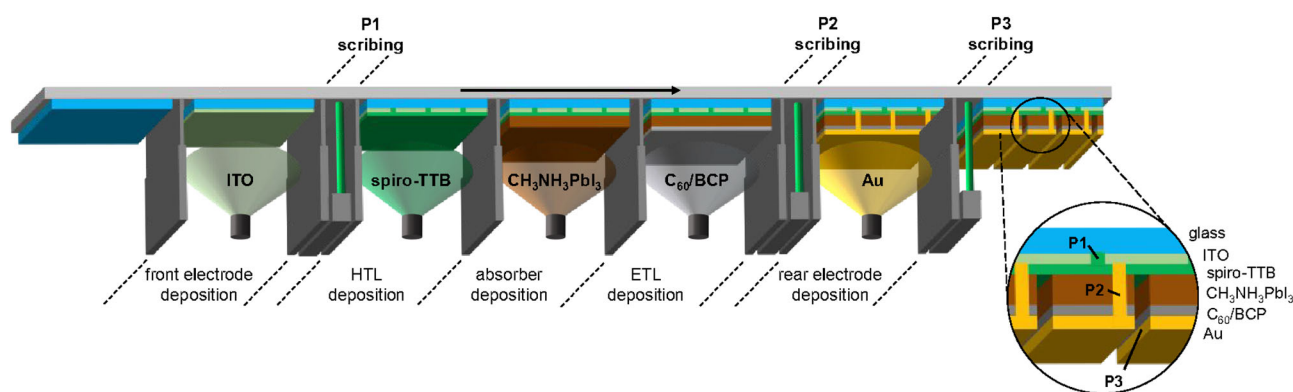

FIGURE 2 Perovskite solar module fabrication based on a potential inline manufacturing process. The inset shows the investigated layer stack sequence employed in this work for the fabrication of all-evaporated perovskite solar modules [Colour figure can be viewed at wileyonlinelibrary.com]

effect on the device's PCE of well below 1%_{rel} decrease, the contact needs to provide a low series resistance via the P2 interconnection line, corresponding to 1 Ω or less for the utilized measurement layout. The correlation of P2 interconnection resistance and expected losses is depicted in Figure S4. This necessitates full removal of the electron transport layer (ETL), the perovskite absorber layer, and the hole transport layer (HTL). Optimizing of fluence and scribing speed, the aspired resistances are achieved for all three scribing lines, being illustrated in Figure 3A–C. For the scribing lines P1 and P3, maximum resistances between adjacent solar cell stripes without damaging the underlying glass substrate and ITO front electrode are achieved in a fluence range of 1.50–3.50 and 0.22–0.45 J cm^{-2} at scanning speeds

of 50 and 100 mm s^{-1}, respectively. Minimal P2 contact resistance down to 0.67 Ω is obtained at fluences of 0.25–0.6 J cm^{-2} and scanning speed of 33 mm s^{-1}. The trends in characteristic resistances correlate well with the scribing line uniformity observed in microscopy images (see Figure S5). These rather broad process windows for each of the scribing lines imply that the process is robust and tolerant against lasing intensity and layer thickness variations, giving sufficient leeway for a reproducible process. The uniform ablation for the individual scribing lines is confirmed by SEM images (see Figure 3D–F), showing clean and debris-free trenches. P1, P2, and P3 scribing lines with lateral extensions of only 60, 50, and 25 μm, respectively, are demonstrated. Supplementary SEM images are depicted in Figure S6.
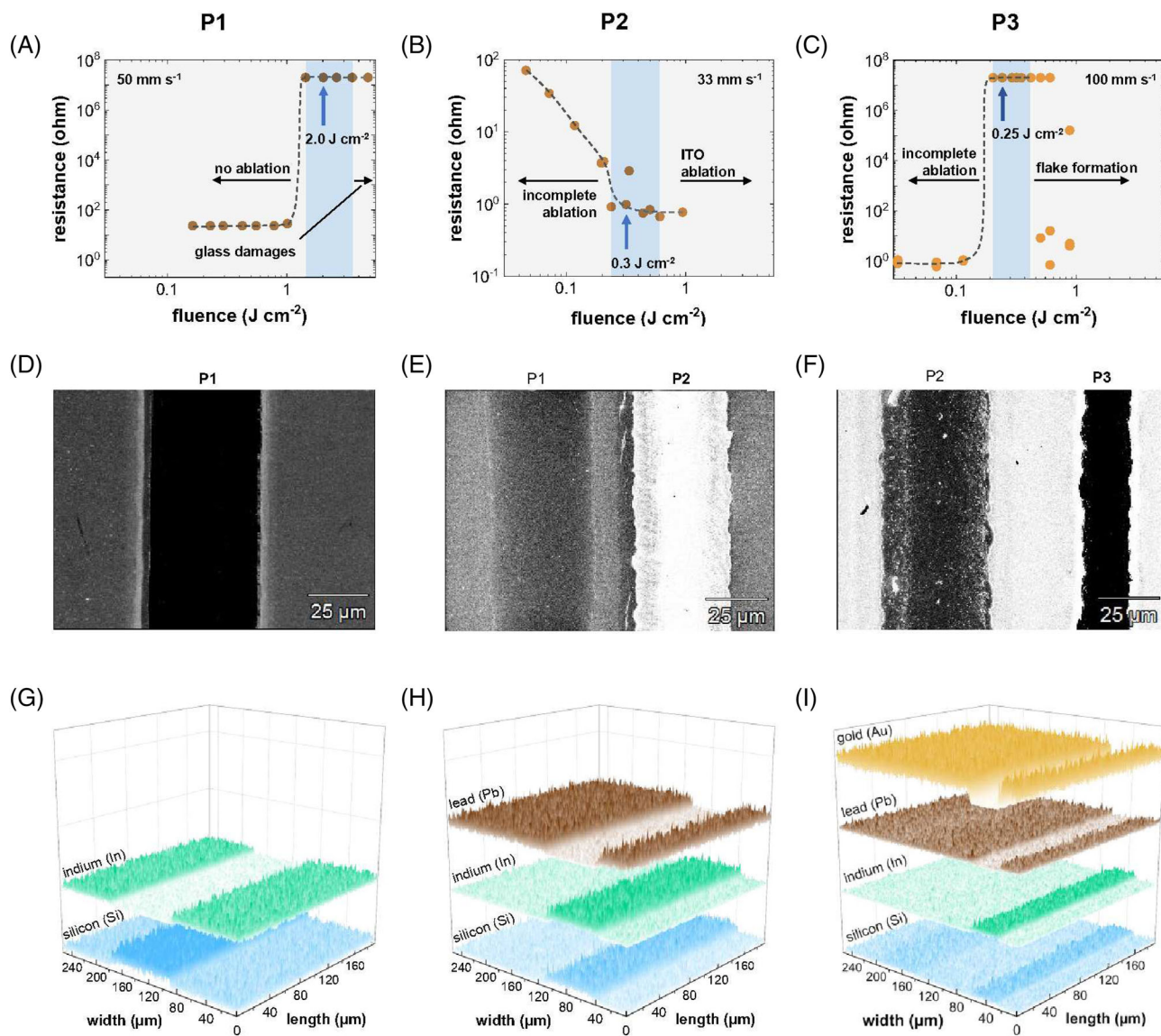

FIGURE 3 Development of high-quality laser scribing lines utilizing only one wavelength of a cost-efficient nanosecond lasing source providing minimal process complexity. (A–C) Optimization of the characteristic resistances of P1, P2, and P3 scribing lines by adjusting the fluence at fixed scribing speed. The highlighted areas illustrate the optimal process window, while the blue arrow marks the chosen scribing parameter for device fabrication in this work. The dashed line connecting data points depicts the trend as guide to the eye. (D–F) SEM images and (G–I) EDX investigations of the individual scribing lines. Amplitude depicts respective element count [Colour figure can be viewed at wileyonlinelibrary.com]

Particularly laser scribing of the P3 scribing line has been reported in literature as challenging due to detrimental debris formation or delamination of the back contact causing shunts in minimodules.[113,118] An optimized parameter set overcomes this challenge as illustrated in Figure S5h. The total inactive interconnection width including alignment tolerances of less than 160 μm is comparable with or even surpasses previously reported laser-scribed interconnections of perovskite minimodules based on multiple laser sources.[59,69,113] The results are further supported by EDX measurements of individual scribing lines. Excellent separation of adjacent solar cell stripes and selective material removal is confirmed through complete removal of ITO and Au, respectively, shown by the distinct reduction in the indium and gold signals (see Figure 3G,I). Likewise, the residual-free interconnection is supported by the negligible lead signal (see Figure 3H), indicating a complete ablation of all functional layers between front and back contact while the underlying ITO layer is not negatively affected.

2.2 | Homogeneous and defect-free large area layer deposition and interconnection

Having developed a laser scribing process that provides uniform, low-resistance module interconnections within comfortable process windows at a single laser wavelength, the scalable deposition of the all-evaporated solar cell layer stack is assessed. PL imaging is employed to assess the material composition and deposition and crystallization homogeneity of the co-evaporated perovskite absorber on substrate areas up to 64 cm², synonymous with a minimodule aperture area of 51 cm² with 18 solar cell stripes (see Figure S7). The P1 and P2 scribing lines are already introduced into the layer stack. The homogeneous deposition of the absorber is achieved over the complete substrate area as shown in Figure 4A. This includes the immediate proximity to the substrate edge, facilitating minimal extent of unusable areas around the edges. The latter is a common problem for solution-based approaches, where edge effects result in
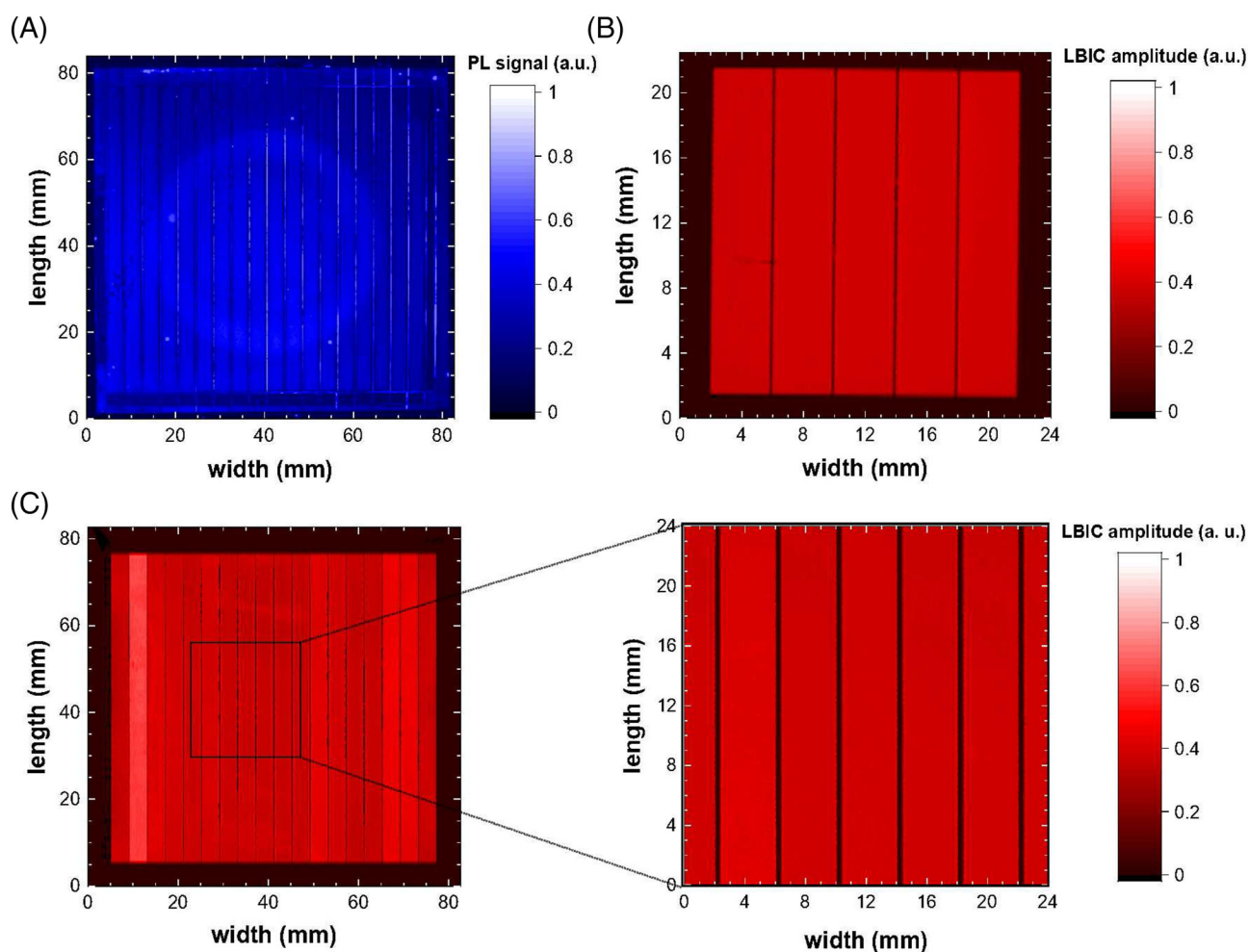

FIGURE 4 Analysis of layer homogeneity and interconnection functionality for all-evaporated all-laser-scribed solar modules. (A) PL imaging of the perovskite absorber deposited on a 64-cm² substrate (51-cm² aperture area) without ETL and back contact but with TCO and HTL. The slightly brighter ring in the center of the substrate is a measurement artifact attributable to the circular excitation illumination of the PL setup. (B) High-resolution LBIC mapping of a 4-cm² aperture area solar module comprised of five interconnected subsolar cells. (C) LBIC mapping of a 51-cm² aperture area solar module consisting of 18 interconnected subsolar cells together with a high-resolution close-up view of the highlighted area. Different scales of the axis should be considered [Colour figure can be viewed at wileyonlinelibrary.com]

inhomogeneous layer deposition close to the substrate edge and thus a reduction of the maximum usable substrate area.[87,119,120] Few defects on the substrate are observed and attributed to crystallization defects caused by dust particles due to the fabrication in a non-cleanroom environment. It should be noted that the slightly brighter ring pattern in the center of the substrate is a measurement artifact attributable to the circular illumination in the PL imaging setup and not a material-related measurement signal.

Combining homogenous absorber deposition of the all-evaporated layer stack and uniform laser scribing, the charge carrier generation and extraction is assessed. Thereby, the homogeneity in photocurrent generation of the all-evaporated all-laser-scribed solar modules is verified in LBIC mapping studies of minimodules with aperture areas of 4 and 51 cm^2.[121] Respective layouts are depicted in Figure S7. Being illustrated in Figure 3B, a minimodule consisting of five interconnected solar cell stripes with a combined aperture area of 4 cm^2 demonstrates a very homogenous charge carrier generation and extraction with only minor handling defects. The uniform signal amplitude within the solar cell stripes confirms the homogeneity of not only the absorber layer but also all functional layers of the layer stack. The latter is of particular importance, as the vapor-based deposition of the absorber on an inhomogeneous (solution-processed) substrate material can also result in inhomogeneous film formation dynamics for the absorber and thus inhomogeneous charge carrier generation and extraction.[117] In addition, uniform signal amplitude across different solar cell stripes further highlights the homogeneous parallel resistance of individual solar cell stripes of the minimodule, demonstrating the high quality of the interconnection process.[121] Furthermore, the LBIC study confirms the low interconnection width of 160 μm synonymous with a GFF as high as 96%. This allows to compete with established thin-film PV and with perovskite minimodules fabricated with picosecond or femtosecond lasers as well as mixed laser and mechanical scribing processes.[24,104,114,122]

Similar homogeneity with only minor variation of parallel resistance is also demonstrated for an increase in aperture area and interconnection line length by more than one decade. This is illustrated in Figure 3C, depicting the LBIC mapping for a minimodule consisting of 18 interconnected solar cell stripes with a total aperture area of a 51 cm^2, where only signal variations of different cell stripes but not within individual cell stripes are visible. A close-up LBIC mapping of the center region of the minimodule, as shown in Figure 3D, reveals similar charge carrier generation homogeneity as was achieved for the 4-cm^2 minimodule with only a slight decrease in GFF to a value of 94%. Thereby, this minimodule significantly surpasses GFFs previously reported by Abzieher et al.[67] and Li et al.[25] for minimodules employing coevaporated perovskite absorbers, while also increasing the device area by up to one decade compared with previous reports. Presented for the first time for all-evaporated perovskite PV devices, the absence of inhomogeneities and signal gradients within cell stripes of the 51-cm^2 module demonstrates the high uniformity and reproducibility of all-evaporated layer stacks independent of substrate dimensions. Having employed identical process parameters for the fabrication of devices of different areas, the high homogeneity of

layer and interconnection fabrication reveals the ease of upscaling of the developed approach for all-evaporated all-laser-scribed minimodules and therefore its excellent transferability to potentially even larger areas.

2.3 | Efficient upscaling of all-laser-scribed all-evaporated perovskite modules

Next, the performance of lab-scale reference solar cells is compared with prototype modules of much larger dimension: Small minimodules consist of five solar cell stripes (each of a size of 0.4 cm × 2 cm) connected in series with a total aperture area of 4.0 cm^2. Largest minimodules consist of 18 solar cell stripes (each of a size of 0.4 cm × 7.1 cm), resulting in a total aperture area of 51.12 cm^2. As illustrated in Figure 1, the latter corresponds to one of the largest minimodules demonstrated in literature with up to four orders of magnitude larger device areas compared with small-area record solar cells commonly reported. Both minimodule designs are based on a cell stripe width of 4 mm (combining the active and interconnection width) with variable lengths, achieving GFFs of 96% and 94% for small and large solar modules, respectively (see Figure S7). In order to ensure comparability between different batches, reference solar cells with active areas of 0.105 cm^2 were processed in parallel. The employed all-evaporated layer stack sequence ITO/spiro-TTB/CH$_3$NH$_3$PbI$_3$/C$_{60}$/BCP/Au was introduced in an earlier work as a high-performance, low-hysteresis architecture with good short-term stability and reproducibility (see Figures S8–S10).[117]

Champion minimodules with an aperture area of 4.0 cm^2 (GFF of 96%) demonstrate PCEs as high as 18.0% with a fill factor (FF) of 81%, an open-circuit voltage (V_{OC}) of 5.5 V, and a short-circuit current density ($J_{SC, cell stripe}$) of 20.2 mA cm^{-2} in backward scan direction. Considering the forward scan direction with PCEs of 17.7%, a FF of 81%, a V_{OC} of 5.5 V, and a $J_{SC, cell stripe}$ of 20.0 mA cm^{-2}, only minimal hysteresis is apparent (see Figure 5A and Table 1). It should be noted that the $J_{SC, cell stripe}$ reported here relates to the aperture area of one solar cell stripe, allowing a better comparison to reference solar cells. The respective performance with regard to the active area is summarized in Table 1. In particular, the high FF and V_{OC} are emphasized, which highlight the high quality of the module interconnection. Compared with the champion reference solar cell with a PCE of 19.3% in backward and 19.2% forward scan direction (see Figures S11 and S12), the PCE loss of only 6.7%$_{rel}$ correlates via GFF with the active area PCE loss of only 2.7%$_{rel}$ (see Figure 5B). Considering the increase by more than one decade in area, this is synonymous with a relative performance loss per decade in area of only 4.3%$_{rel}$/dec. The loss attributed to the GFF accounts for the largest proportion of 2.5%$_{rel}$/dec, as the interconnection area had to be introduced as an increment of fixed minimal width for a relatively small upscaling. Loss mechanisms related to the upscaling itself (e.g., interconnection damages, increased resistances, or defects and inhomogeneities in the upscaled layers) result in total to a minimal loss of only 1.7%$_{rel}$/dec. Compared with our earlier work (GFF of 19.5%$_{rel}$/dec, other upscaling
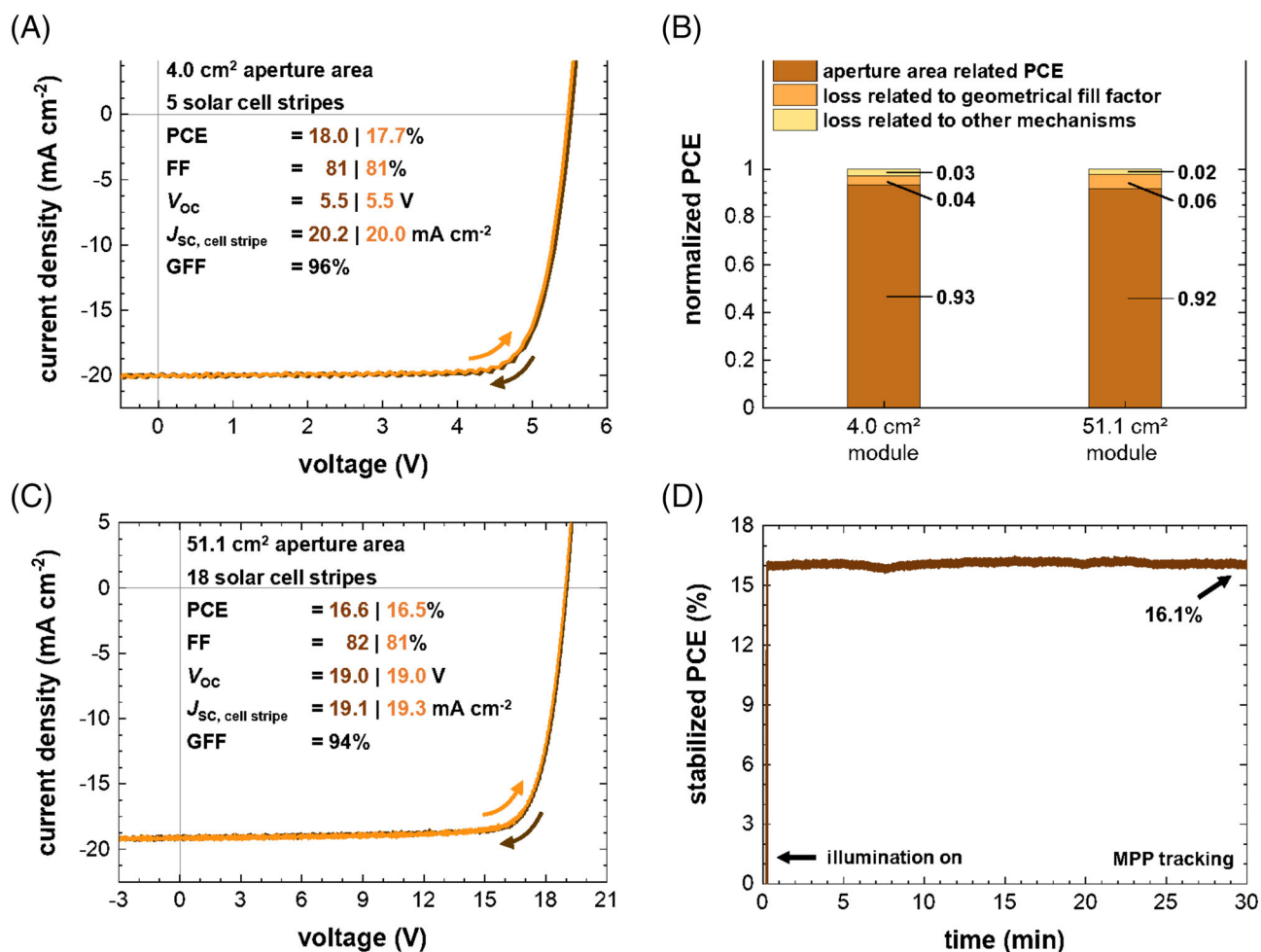
(A)

(B)

(C)

(D)

FIGURE 5 Device performance of all-evaporated all-laser-scribed solar modules with different device areas. J-V characteristics of all-evaporated all-laser-scribed perovskite modules with aperture areas of 4.0 cm^2 (A) and 51.1 cm^2 (C), consisting of 5 and 18 monolithically interconnected solar cell stripes, respectively. (B) Comparison of the upscaling losses for mini-modules of different device areas. The values are normalized with regard to the performance of the small-area reference solar cells (0.105 cm^2). (D) Short-term stability under continuous illumination during MPP tracking for the champion mini-module with 51.1 cm^2 aperture area. MPP tracking is performed at normal operating cell temperature (NOCT) conditions without active cooling of the mini-module [Colour figure can be viewed at wileyonlinelibrary.com]

TABLE 1 Comparison of aperture and active area solar module parameters extracted from backward (forward) J–V scans of all-evaporated all-laser-scribed perovskite solar modules with different device areas

Aperture area (cm^2)	GFF (%)	Aperture area values						Active area values		
		PCE (%)	FF (%)	V_{OC} (V)	$J_{SC, cell}$ (mA cm^{-2})	$J_{SC, module}$ (mA cm^{-2})	I_{SC} (mA)	PCE (%)	$J_{SC, cell}$ (mA cm^{-2})	$J_{SC, module}$ (mA cm^{-2})
4.0	96	18.0 (17.7)	81.0 (81.0)	5.5 (5.5)	20.2 (20.0)	4.0 (4.0)	16.1 (16.0)	18.8 (18.4)	21.0 (20.8)	4.2 (4.2)
51.1	94	16.6 (16.5)	82.0 (81.0)	19.0 (19.0)	19.1 (19.3)	1.1 (1.1)	51.1 (54.7)	17.6 (17.5)	20.3 (20.5)	1.1 (1.1)

losses of 9.8%$_{rel}$/dec) as well as other literature,[117] this is a very significant progress.

Demonstrating the efficient upscaling process on even larger device areas, minimodules with aperture areas of 51.1 cm^2 (GFF of 94%) are discussed next. Champion solar modules achieve PCEs as high as 16.6% with a FF of 82%, a V_{OC} of 19.0 V, and a $J_{SC, cell stripe}$ of 19.1 mA cm^{-2} in backward scan direction and PCEs of 16.5% with a FF of 81%, a V_{OC} of 19.0 V and a $J_{SC, cell stripe}$ of 19.3 mA cm^{-2} in forward scan direction (see Figure 5C and Table 1). Again, the obtained

FF and V_{OC} highlight the high quality of the module fabrication. In addition, to the authors' best knowledge, the herein demonstrated devices are the best perovskite minimodules with aperture areas above 50 cm^2 demonstrated in research at the time of writing (see also Figure 1 and Table S1). Slightly lower performance values compared with the smaller minimodules are mainly explained by the reduction of GFF and the slightly lower performance of the deposition process, with reference solar cells exhibiting PCEs of 18.1% in backward and 17.9% in forward scan direction (see Figures S11 and S12).

Considering relative PCE losses (see Figure 5B) and upscaled area, even smaller upscaling losses of 3.1%$_{rel}$/dec are obtained for these larger minimodules, with an influence of the GFF of 2.2%$_{rel}$/dec and only 0.9%$_{rel}$/dec loss due to other mechanisms. In addition, the all-evaporated solar modules exhibit stable power output with a stabilized PCE of up to 16.1% after 30 min of maximum power point (MPP) tracking (see Figure 5D). The slight reduction in stabilized PCE is a result of the MPP tracking under nominal operating cell temperature (NOCT) conditions without any active cooling. Nevertheless, similar short-term stability is achieved for the small-area solar cells tracked under standard test conditions (STC) (see also Figure S8).

In the following, the above-reported performance of all-evaporated perovskite solar modules is put in context to the performance of state-of-the-art perovskite minimodules reported in literature (see Table S2). Figure 6 illustrates that upscaling losses in the all-evaporated approach are highly reduced compared with the significantly more extensively investigated solution-based approaches. The lower upscaling losses are in part attributable to the excellent homogeneity of the deposition of all functional layers via vapor-based deposition methods, resulting from a far simpler upscaling process than for solution-based approaches. While losses related to the GFF have only slightly improved, the fabrication of state-of-the-art interconnections via facile laser scribing process utilizing an industrially viable nanosecond laser needs to be stressed. In combination, upscaling losses of only 3.1%$_{rel}$/dec are achieved here, a significant improvement to the already published current champion minimodules demonstrated by both Dai et al. and Ren et al. for blade-coated

(7.2%$_{rel}$/dec) and spin-coated (6.9%$_{rel}$/dec) perovskite minimodules, respectively. It should be further noted that the presented perovskite minimodule area was more than doubled compared with the champion minimodule of Ren et al. The presented results denote also an important progress for the vapor-processed perovskite solar modules in general, both within our group and compared with the previously reported minimodules. Li et al. employed vapor processing for the deposition of the perovskite absorber while all charge selective transport layers were prepared via solution-based methods, upscaling losses of 12.1%$_{rel}$/dec and 3.3%$_{rel}$/dec attributed to the GFF and to other mechanisms, respectively, were demonstrated. The improvement achieved with our employed all-evaporated layer stack further highlights the prospects of an all-vapor-based layer fabrication. Most importantly, upscaling-related losses of perovskite PV are reduced here for the first time to values of established PV technologies, being an important step for the perovskite-based technology in general and its prospects for future commercialization. In particular, the upscaling losses reported here for all-evaporated perovskite solar modules are comparable with CIGS and CdTe thin-film modules that are also reliant on vapor-based deposition techniques.

The achieved cell-to-module active area PCE loss of only 2.3%$_{rel}$ are in very good agreement with the predicted losses of the theoretical model of Di Giacomo et al. (2%$_{rel}$).[59] The accurate prediction of active area PCE losses, originating from resistive losses, proves that losses caused by upscaling-related inhomogeneities are insignificant for vapor-based deposition. Hence, based on the area-independent resistive losses, as well as the negligible losses due to
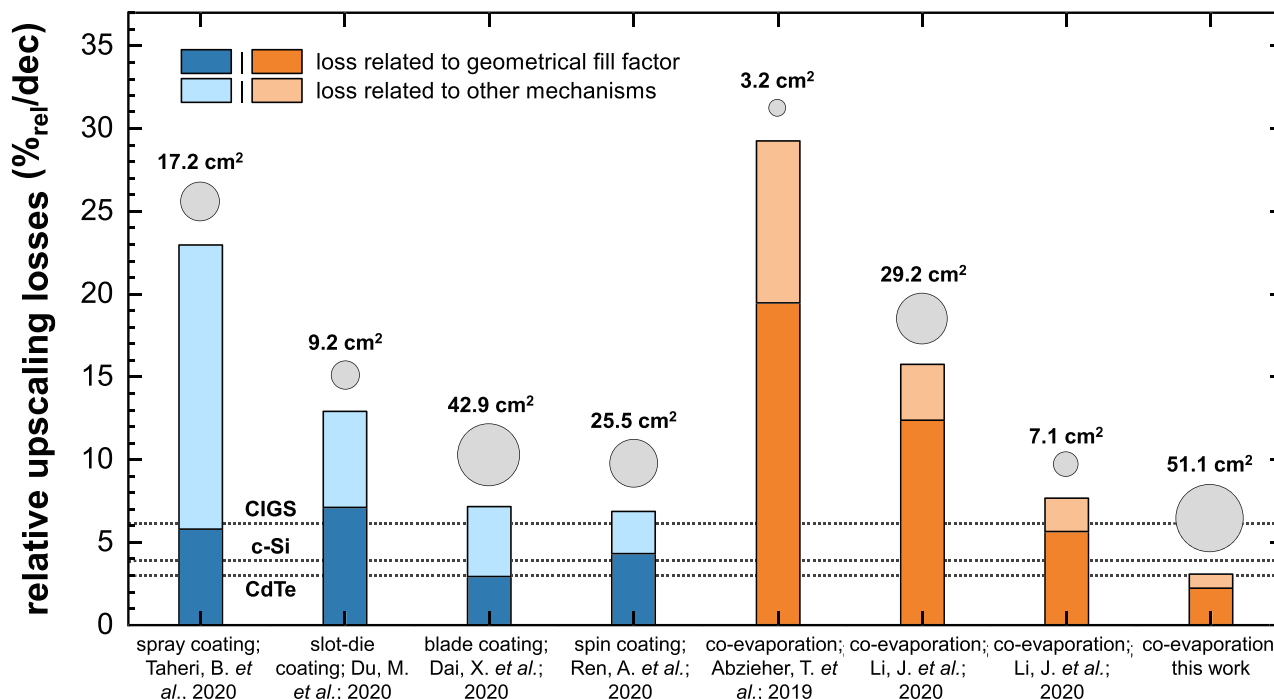

FIGURE 6 Comparison of relative upscaling losses per decade of upscaled area (dec) for recently reported perovskite solar modules utilizing different fabrication techniques. Gray circles illustrate the achieved maximum aperture areas of the respective solar modules. Background values highlight the upscaling losses commonly achieved for monocrystalline silicon, CdTe, and CIGS solar modules[5,24,25,43,67,69,70,77] [Colour figure can be viewed at wileyonlinelibrary.com]

inhomogeneities, the non-GFF-related losses are expected to remain constant at around 2%$_{rel}$ for further upscaling in area. Therefore, the upscaling to even larger areas, being possible with larger evaporation systems, is not expected to result in major differences in upscaling efficiency, given the high homogeneity of layer deposition and interconnection fabrication.[24,25,71,123–125] This is also indicated by achieving similar upscaling efficiencies for 4- and 51-cm^2 devices. While GFF-related losses increased to 6% for the 51-cm^2 module, further adjustments such as the reduction of distance between the individual scribing lines is expected to reduce this loss to at least 4% as demonstrated for the 4-cm^2 minimodules. In that regard, the concept of point interconnections recently introduced by Rakocevic et al. for perovskite minimodules might also be of significant interest for further development.[102] Furthermore, the strong analogy of the developed approach to the manufacturing of established thin-film technologies potentially benefits further upscaling via knowledge transfer. For instance, the common utilization of additional scanner lens systems to increase module width and throughput is expected to enable the fabrication of modules of several hundred square centimeters with GFFs of 96% or above.[126]

3 | CONCLUSION

This work reports on all-evaporated perovskite solar modules, highlighting the upscaling of this technology over several orders of magnitude of device area with very low upscaling losses. Combining an all-evaporated perovskite solar cell architecture with a 532-nm nanosecond laser scribing system suitable for the processing of all three interconnection lines at scribing speeds of up to 100 mm s^{-1}, interconnections with minimal total lateral extension of down to 160 μm and excellent electrical properties are processed. High homogeneity of the all-evaporated perovskite solar module layer stack during upscaling to 51.1 cm^2 (by a factor of 500) is demonstrated in PL images and LBIC mappings, emphasizing the ease of homogenous device fabrication when using exclusively vapor-based deposition techniques. Prototype solar modules achieve PCEs of up to 18.0% and 16.6% for aperture areas of 4.0 and 51.1 cm^2, respectively. To the authors' best knowledge, the latter represents the highest reported PCE for an all-evaporated solar module of similar size. The comparison of the achieved upscaling losses of only 3.1%$_{rel}$/dec of upscaled area with other upscaling approaches as well as established thin-film PV technologies like CIGS, c-Si, and CdTe highlights the excellent upscaling efficiency of the developed process.

4 | EXPERIMENTAL SECTION

4.1 | Substrate preparation

Following the established superstrate configuration of perovskite solar cells, fabrication of all investigated devices utilized purchased glass substrates coated with ITO (Luminescence Technology, CAS:

50926-11-9). For solar modules, substrate sizes of 30 × 30 mm^2, 80 × 80 mm^2, and 100 × 100 mm^2 were used and laser scribed as discussed below. Reference solar cells were fabricated onto 16 × 16 mm^2 glass substrates with prepatterned ITO.

4.2 | Solar cell and module fabrication

The employed layer stack sequence ITO/spiro-TTB/CH$_3$NH$_3$PbI$_3$/C$_{60}$/BCP/Ag for the all-evaporated solar cells and modules was discussed in detail in a previous publication.[117] Glass substrates coated with prepatterned ITO were cleaned in acetone and isopropanol in an ultrasonic bath for 10 min each, followed by an additional cleaning step in an oxygen plasma for 3 min immediately before the deposition of the first charge transport layer. Afterwards, substrates were transferred into a nitrogen-filled glovebox for the deposition of the functional layers without further exposure to air. The <5-nm-thick 2,2′,7,7′-tetra(N,N-di-p-tolyl)amino-9,9-spirobifluorene (spiro-TTB, Luminescence Technology, CAS: 515834-67-0) was thermally evaporated in an OPTIvap evaporation system (CreaPhys GmbH) without any doping. The perovskite absorber was fabricated by co-evaporation of lead iodide (PbI$_2$, TCI Deutschland GmbH, 99.99% purity, CAS: 10101-63-0) and methylammonium iodide (CH$_3$NH$_3$I, Luminescence Technology, >99.5% purity, CAS: 14965-49-2) in a PEROvap evaporations system (CreaPhys GmbH). PbI$_2$ was used for several consecutive evaporation runs while CH$_3$NH$_3$I was replaced after every deposition. Substrates and materials were kept in high vacuum overnight for outgassing. In order to prevent a strong rise in CH$_3$NH$_3$I background pressure and to facilitate rate detection, the evaporation system was equipped with cooling shields around the evaporation sources cooled to a temperature below −15°C. PbI$_2$ was evaporated at an evaporation rate of 1.5 Å s^{-1}, CH$_3$NH$_3$I at an evaporation rate between 2.0 and 2.5 Å s^{-1}. Substrates were kept at a temperature of 25°C during deposition. After deposition of the absorber, samples were transferred back to the previous evaporation system for the deposition of a 25-nm-thick C$_{60}$ fullerene layer (Alfa Aesar, 98%, CAS: 99685-96-8) and a 6-nm-thick bathocuproine layer (BCP, Luminescence Technology, CAS: 4733-39-5). As back contact, a 75- to 100-nm-thick gold or silver layer was used that was deposited in the same evaporation system. Reference solar cells were evaporated using a metal mask, resulting in a device area of 0.105 cm^2.

4.3 | Laser scribing

For scribing of the individual scribing lines P1, P2, and P3, a custom-built laser scribing setup was used (Bergfeld Lasertech GmbH). The setup employed a 1-ns Nd:YVO$_4$ laser (Picolo AOT 10-MOPA, InnoLas Laser GmbH) with a wavelength of 1064 and 532 nm, variable frequency and power output, a scanner system, a camera, and an air ventilation and filtering circuit. In order to prevent any contact to ambient atmosphere, the system was incorporated in a nitrogen-filled glovebox. Accurate dimensions were ensured by calibrating scribing

layouts via an optical microscope (Leitz Wetzlar). Patterning followed the scribing layout shown in Figure S7. The P1 scribing process was carried out before deposition of the first charge transport layer (spiro-TTB) to guarantee a homogeneous film formation of the vapor-processed perovskite absorber, utilizing a scribing speed of 50 mm s^{-1} and a laser pulse fluence of with 2 J cm^{-2}. A reference mark was ablated for subsequent alignment of P2 and P3 scribing lines. After deposition of all functional layers including the second charge transport layer (C$_{60}$/BCP) and alignment with the reference mark, the P2 lines were scribed at a speed of 33 mm s^{-1} and a laser pulse fluence of 0.35 J cm^{-2}. Finally, after deposition of the rear electrode and alignment, the P3 lines were scribed at a scribing speed of 100 mm s^{-1} and laser pulse fluence of 0.3 J cm^{-2}. All scribing lines were fabricated at a laser pulse frequency of 10 kHz from the film side.

4.4 | Characterization

SEM and EDX spectroscopy investigations were performed in a Zeiss LEO1530 scanning electron microscope with in-lens and EDX detector. In order to prevent charge up of the glass substrate during the investigation of the P1 scribing line, the substrate was covered with a 3-nm-thick sputtered layer of platinum before investigation. Microscopy images were taken by a BH2-UMA (Olympus Corporation). A 2.1-megapixel scientific CMOS camera (Quantalux sCMOS Camera by Thorlabs) was used to detect the PL signal, yielding spatially resolved PL images. A 470-nm excitation LED ring (HPR2 by CCS Inc.) was utilized as illumination source. The residual excitation light was filtered out by placing a 780-nm longpass filter (FGL780S by Thorlabs) in front of the camera. All measurements were performed in ambient air. Laser beam-induced current (LBIC) mapping was conducted in a custom-built setup employing a continuous 532-nm laser for illumination, a chopper and lock-in amplifier (SR830, Stanford Research Systems) operating at 66 Hz for signal enhancement, and a motorized sample stage for scanning. In order to avoid degradation during LBIC measurements, devices were flushed with a continuous stream of nitrogen. x and y resolutions corresponded to 0.1 and 1.0 mm for standard measurements, respectively, and to 0.1 and 0.2 mm for high-resolution measurements. Current–density–voltage (J–V) measurements were carried out in a solar simulator (Newport Oriel Sol3A) under global standard AM1.5G radiation, whose intensity was calibrated with a silicon reference solar cell equipped with a KG5 short pass filter. Scans were performed in forward and backward direction at a scanning speed of about 0.6 V s^{-1}. Continuous measurements of the MPP were conducted by using a perturb-and-observe algorithm. For small-area reference cells, the temperature was kept constant at 25°C by utilizing a microcontroller regulated Peltier element. Solar modules were not actively cooled during measurement.

CONFLICT OF INTEREST

There are no conflicts to declare.

AUTHOR CONTRIBUTIONS

The present manuscript was written through contributions of all mentioned authors. David B. Ritzer (development of module interconnection) and Tobias Abzieher (development of all-evaporated perovskite solar cells) contributed equally to this work and share first authorship.

DATA AVAILABILITY STATEMENT

The data that support the findings of this study are available from the corresponding author upon reasonable request.

ORCID

David B. Ritzer https://orcid.org/0000-0002-3301-6688
Bryce S. Richards https://orcid.org/0000-0001-5469-048X

REFERENCES

1. Sutherland Brandon R, Sargent Edward H. Perovskite photonic sources. *Nature Photonics*. 2016;10(5):295-302. https://doi.org/10.1038/nphoton.2016.62
2. Jena AK, Kulkarni A, Miyasaka T. Halide perovskite photovoltaics: background, status, and future prospects. *Chem Rev*. 2019;119(5):3036-3103.
3. De Wolf S, Holovsky J, Moon SJ, et al. Organometallic halide perovskites: sharp optical absorption edge and its relation to photovoltaic performance. *J Phys Chem Lett*. 2014;5(6):1035-1039.
4. National Renewable Energy Laboratory 2021, Best Research-Cell Efficiencies. https://www.nrel.gov/pv/cell-efficiency.html (accessed April 2021).
5. Green M, Dunlop E, Hohl-Ebinger J, Yoshita M, Kopidakis N, Hao X. Solar cell efficiency tables (version 57). *Prog Photovoltaics Res Appl*. 2021;29(1):3-15.
6. Galagan Y. Perovskite solar cells: toward industrial-scale methods. *J Phys Chem Lett*. 2018;9(15):4326-4335.
7. Correa-Baena JP, Saliba M, Buonassisi T, et al. Promises and challenges of perovskite solar cells. *Science (80-.)*. 2017;358(6364):739-744.
8. Niu G, Guo X, Wang L. Review of recent progress in chemical stability of perovskite solar cells. *J Mater Chem A*. 2015;3(17):8970-8980.
9. Ke W, Kanatzidis MG. Prospects for low-toxicity lead-free perovskite solar cells. *Nat Commun*. 2019;10(1):1-4.
10. Salhi B, Wudil YS, Hossain MK, Al-Ahmed A, Al-Sulaiman FA. Review of recent developments and persistent challenges in stability of perovskite solar cells. *Renew Sustain Energy Rev*. 2018;90:210-222.
11. Snaith HJ. Present status and future prospects of perovskite photovoltaics. *Nat Mater*. 2018;17(5):372-376.
12. Saliba M, Correa-Baena JP, Wolff CM, et al. How to make over 20% efficient perovskite solar cells in regular (n–i–p) and inverted (p–i–n) architectures. *Chem Mater*. 2018;30(13):4193-4201.

13. Jiang Q, Zhao Y, Zhang X, et al. Surface passivation of perovskite film for efficient solar cells. *Nat Photonics*. 2019;13(7):460-466.

14. Jeong M, Choi IW, Go EM, et al. Stable perovskite solar cells with efficiency exceeding 24.8% and 0.3-V voltage loss. *Science (80-.)*. 2020;369:1615-1620.

15. Lee SW, Bae S, Kim D, Lee HS. *Adv Mater*. 2020;32(51):2002202.

16. Uličná S, Dou B, Kim DH, et al. Scalable deposition of high-efficiency perovskite solar cells by spray-coating. *ACS Appl Energy Mater*. 2018; 1(5):1853-1857.

17. Yang M, Li Z, Reese MO, et al. Perovskite ink with wide processing window for scalable high-efficiency solar cells. *Nat Energy*. 2017; 2(5):1-9.

18. Dai X, Deng Y, van Brackle CH, Huang J. Meniscus fabrication of halide perovskite thin films at high throughput for large area and low-cost solar panels. *Int J Extrem Manuf*. 2019;1(2):022004. https://doi.org/10.1088/2631-7990/ab263e

19. Deng Y, Xu S, Chen S, Xiao X, Zhao J, Huang J. Defect compensation in formamidinium–caesium perovskites for highly efficient solar mini-modules with improved photostability. *Nat Energy*. 2021;6(6): 633-641.

20. Di Giacomo F, Fledderus H, Gorter H, et al. Large area >140 cm² perovskite solar modules made by sheet to sheet and roll to roll fabrication with 14.5% efficiency. *2018 IEEE 7th World Conf Photovolt Energy Conversion, WCPEC 2018−A Jt Conf 45th IEEE PVSC, 28th PVSEC 34th EU PVSEC*. 2018;2795-2798.

21. Mei A, Li X, Liu L, et al. A hole-conductor–free, fully printable mesoscopic perovskite solar cell with high stability. *Science (80-.)*. 2014;345(6194):295-298.

22. Di Giacomo F, Shanmugam S, Fledderus H, et al. Up-scalable sheet-to-sheet production of high efficiency perovskite module and solar cells on 6-in. substrate using slot die coating. *Sol Energy Mater Sol Cells*. 2018;181:53-59.

23. Yao J, Yang L, Cai F, et al. The impacts of PbI₂ purity on the morphology and device performance of one-step spray-coated planar heterojunction perovskite solar cells. *Sustain Energy Fuels*. 2018;2(2): 436-443.

24. Li J, Dewi HA, Wang H, et al. Design of perovskite thermally co-evaporated highly efficient mini-modules with high geometrical fill factors. *Sol RRL*. 2020;4(12):2000473.

25. Li J, Wang H, Chin XY, et al. Highly efficient thermally co-evaporated perovskite solar cells and mini-modules. *Joule*. 2020;4(5): 1035-1053.

26. Remeika M, Raga SR, Zhang S, Qi Y. Transferrable optimization of spray-coated PbI2films for perovskite solar cell fabrication. *J Mater Chem A*. 2017;5(12):5709-5718.

27. Matteocci F, Razza S, Di Giacomo F, et al. Solid-state solar modules based on mesoscopic organometal halide perovskite: a route towards the up-scaling process. *Phys Chem Chem Phys*. 2014;16(9): 3918-3923.

28. Lan DH, Hong SH, Chou LH, Wang XF, Liu CL, Power J. High throughput two-step ultrasonic spray deposited CH3NH3PbI3 thin film layer for solar cell application. *Sources*. 2018;390:270-277.

29. Vesce L, Stefanelli M, Herterich JP, et al. Ambient air blade-coating fabrication of stable triple-cation perovskite solar modules by green solvent quenching. *Sol RRL*. 2021;5(8):2100073.

30. Ouyang Z, Yang M, Whitaker JB, Li D, van Hest MFAM. Toward scalable perovskite solar modules using blade coating and rapid thermal processing. *ACS Appl Energy Mater*. 2020;3(4):3714-3720.

31. Ji R, Zhang Z, Cho C, et al. Thermally evaporated methylammonium-free perovskite solar cells. *J Mater Chem C*. 2020;8(23):7725-7733.

32. Grancini G, Roldán-Carmona C, Zimmermann I, et al. One-year stable perovskite solar cells by 2D/3D interface engineering. *Nat Commun*. 2017;8(1):1-8.

33. Küffner J, Wahl T, Schultes M, et al. Nanoparticle wetting agent for gas stream-assisted blade-coated inverted perovskite solar cells and modules. *ACS Appl Mater Interfaces*. 2020;12(47):52678-52690.

34. Li H, Bu T, Li J, et al. Ink engineering for blade coating FA-dominated perovskites in ambient air for efficient solar cells and modules. *ACS Appl Mater Interfaces*. 2021;13(16):18724-18732.

35. Jeon NJ, Na H, Jung EH, et al. A fluorene-terminated hole-transporting material for highly efficient and stable perovskite solar cells. *Nat Energy*. 2018;3(8):682-689.

36. Yang Z, Zhang W, Wu S, et al. Slot-die coating large-area formamidinium-cesium perovskite film for efficient and stable parallel solar module. *Sci Adv*. 2021;7(18):eabg3749.

37. Qiu S, Xu X, Zeng L, et al. Biopolymer passivation for high-performance perovskite solar cells by blade coating. *Chem*. 2020;54: 45-52.

38. Matteocci F, Vesce L, Utama Kosasih F, et al. Fabrication and morphological characterization of high-efficiency blade-coated perovskite solar modules. *ACS Appl Mater Interfaces*. 2019;11(28):25195-25204. https://doi.org/10.1021/acsami.9b05730

39. Kim B, Ko SG, Sonu KS, Ri JH, Kim UC, Il Ryu G. Effects of adding PbI₂ on the performance of hole-transport material-free mesoscopic perovskite solar cells with carbon electrode. *J Electron Mater*. 2018; 47(10):6266-6271.

40. Verma A, Martineau D, Abdolhosseinzadeh S, Heier J, Nüesch F. Inkjet printed mesoscopic perovskite solar cells with custom design capability. *Mater Adv*. 2020;1(2):153-160.

41. Subbiah AS, Isikgor FH, Howells CT, et al. High-performance perovskite single-junction and textured perovskite/silicon tandem solar cells via slot-die-coating. *ACS Energy Lett*. 2020;5(9):3034-3040.

42. Xu M, Ji W, Sheng Y, et al. Efficient triple-mesoscopic perovskite solar mini-modules fabricated with slot-die coating. *Nano Energy*. 2020;74:104842.

43. Dai X, Deng Y, Van Brackle CH, et al. Scalable fabrication of efficient perovskite solar modules on flexible glass substrates. *Adv Energy Mater*. 2020;10(1):1903108. https://doi.org/10.1002/aenm. 201903108

44. Deng Y, Wang Q, Yuan Y, Huang J. Vividly colorful hybrid perovskite solar cells by doctor-blade coating with perovskite photonic nanostructures. *Mater Horizons*. 2015;2(6):578-583.

45. Tait JG, Manghooli S, Qiu W, et al. Rapid composition screening for perovskite photovoltaics via concurrently pumped ultrasonic spray coating. *J Mater Chem A*. 2016;4(10):3792-3797.

46. Kim YY, Yang T-Y, Suhonen R, et al. Gravure-printed flexible perovskite solar cells: toward roll-to-roll manufacturing. *Adv Sci*. 2019; 6(7):1802094.

47. Gharibzadeh S, Abdollahi Nejand B, Jakoby M, et al. Perovskite solar cells: record open-circuit voltage wide-bandgap perovskite solar cells utilizing 2D/3D perovskite heterostructure. *Adv Energy Mater*. 2019; 9(21):1970079.

48. Gheno A, Huang Y, Bouclé J, et al. Toward highly efficient inkjet-printed perovskite solar cells fully processed under ambient conditions and at low temperature. *Sol RRL*. 2018;2(11):1800191.

49. Huckaba AJ, Lee Y, Xia R, et al. Inkjet-printed mesoporous TiO₂ and perovskite layers for high efficiency perovskite solar cells. *Energ Technol*. 2019;7(2):317-324.

50. Heo JH, Lee MH, Jang MH, Im SH. Highly efficient CH₃NH₃PbI₃₋ₓClₓ mixed halide perovskite solar cells prepared by re-dissolution and crystal grain growth via spray coating. *J Mater Chem A*. 2016; 4(45):17636-17642.

51. Hu Y, Si S, Mei A, et al. Front Cover: Solar RRL 2/2017. *Sol RRL*. 2017;1(2):1770106.

52. Deng Y, Zheng X, Bai Y, Wang Q, Zhao J, Huang J. Surfactant-controlled ink drying enables high-speed deposition of perovskite

films for efficient photovoltaic modules. *Nat Energy*. 2018;3(7):560-566.

53. Galagan Y, Di Giacomo F, Gorter H, et al. Roll-to-roll slot die coated perovskite for efficient flexible solar cells. *Adv Energy Mater*. 2018;8(32):1801935. https://doi.org/10.1002/aenm.201801935

54. Raminafshar C, Dracopoulos V, Mohammadi MR, Lianos P. Carbon based perovskite solar cells constructed by screen-printed components. *Electrochim Acta*. 2018;276:261-267.

55. Mishra A, Ahmad Z, Zimmermann I, et al. Effect of annealing temperature on the performance of printable carbon electrodes for perovskite solar cells. *Org Electron*. 2019;65:375-380.

56. Yang M, Hoe Kim D, Klein TR, et al. Highly efficient perovskite solar modules by scalable fabrication and interconnection optimization. *ACS Energy Lett*. 2018;3(2):322-328. https://doi.org/10.1021/acsenergylett.7b01221

57. Razza S, Di Giacomo F, Matteocci F, et al. Perovskite solar cells and large area modules (100 cm^2) based on an air flow-assisted PbI$_2$ blade coating deposition process. *Sources*. 2015;277:286-291.

58. Zhu X, Du M, Feng J, et al. High-efficiency perovskite solar cells with imidazolium-based ionic liquid for surface passivation and charge transport. *Angew Chemie Int Ed*. 2020;60(8):4238-4244. https://doi.org/10.1002/anie.202010987

59. Di Giacomo F, Castriotta LA, Kosasih FU, Di Girolamo D, Ducati C, Di Carlo A. Upscaling inverted perovskite solar cells: optimization of laser scribing for highly efficient mini-modules. *Micromachines*. 2020;11(12):1127.

60. Li P, Liang C, Bao B, et al. Inkjet manipulated homogeneous large size perovskite grains for efficient and large-area perovskite solar cells. *Nano Energy*. 2018;46:203-211.

61. Bishop JE, Mohamad DK, Wong-Stringer M, Smith A, Lidzey DG. Spray-cast multilayer perovskite solar cells with an active-area of 1.5 cm^2. *Sci Rep*. 2017;7(1):1-11.

62. Deng Y, Peng E, Shao Y, Xiao Z, Dong Q, Huang J. Scalable fabrication of efficient organolead trihalide perovskite solar cells with doctor-bladed active layers. *Energ Environ Sci*. 2015;8(5):1544-1550.

63. Niu T, Lu J, Tang MC, et al. High performance ambient-air-stable FAPbI$_3$ perovskite solar cells with molecule-passivated Ruddlesden–Popper/3D heterostructured film. *Energ Environ Sci*. 2018;11(12):3358-3366.

64. Li J, Dagar J, Shargaieva O, et al. 20.8% slot-die coated MAPbI$_3$ perovskite solar cells by optimal DMSO-content and age of 2-ME based precursor inks. *Adv Energy Mater*. 2021;11(10):2003460. https://doi.org/10.1002/aenm.202003460

65. Kim JE, Jung YS, Heo YJ, et al. Slot die coated planar perovskite solar cells via blowing and heating assisted one step deposition. *Sol Energy Mater Sol Cells*. 2018;179:80-86.

66. Burkitt D, Searle J, Watson T. Perovskite solar cells in N-I-P structure with four slot-die-coated layers. *R Soc Open Sci*. 2018;5(5):172158. https://doi.org/10.1098/rsos.172158

67. Abzieher T, Moghadamzadeh S, Schackmar F, et al. Electron-beam-evaporated nickel oxide hole transport layers for perovskite-based photovoltaics. *Adv Energy Mater*. 2019;9(12):1802995.

68. Schlisske S, Mathies F, Busko D, et al. Design and color flexibility for inkjet-printed perovskite photovoltaics. *ACS Appl Energy Mater*. 2019;2(1):764-769.

69. Du M, Zhu X, Wang L, et al. High-pressure nitrogen-extraction and effective passivation to attain highest large-area perovskite solar module efficiency. *Adv Mater*. 2020;32(47):2004979.

70. Ren A, Lai H, Hao X, et al. Efficient perovskite solar modules with minimized nonradiative recombination and local carrier transport losses. *Joule*. 2020;4(6):1263-1277.

71. Abzieher T, Schwenzer JA, Moghadamzadeh S, et al. Efficient all-evaporatedpin-perovskite solar cells: a promising approach toward industrial large-scale fabrication. *IEEE J Photovoltaics*. 2019;9(5):1249-1257.

72. Bishop JE, Read CD, Smith JA, Routledge TJ, Lidzey DG. Fully spray-coated triple-cation perovskite solar cells. *Sci Rep*. 2020;10(1):1-8.

73. Dou B, Whitaker JB, Bruening K, et al. Roll-to-roll printing of perovskite solar cells. *ACS Energy Lett*. 2018;3(10):2558-2565.

74. Verma A, Martineau D, Hack E, et al. Towards industrialization of perovskite solar cells using slot die coating. *J Mater Chem C*. 2020;8(18):6124-6135.

75. Chou LH, Wang XF, Osaka I, Wu CG, Liu CL. Scalable ultrasonic spray-processing technique for manufacturing large-area CH$_3$NH$_3$PbI$_3$ perovskite solar cells. *ACS Appl Mater Interfaces*. 2018;10(44):38042-38050.

76. Ru P, Bi E, Zhang Y, et al. High electron affinity enables fast hole extraction for efficient flexible inverted perovskite solar cells. *Adv Energy Mater*. 2020;10(12):1903487.

77. Taheri B, Calabrò E, Matteocci F, et al. Automated scalable spray coating of SnO$_2$ for the fabrication of low-temperature perovskite solar cells and modules. *Energ Technol*. 2020;8(5):1901284.

78. You Y, Tian W, Min L, Cao F, Deng K, Li L. TiO$_2$/WO$_3$ bilayer as electron transport layer for efficient planar perovskite solar cell with efficiency exceeding 20%. *Adv Mater Interfaces*. 2020;7(1):1901406.

79. Gardner KL, Tait JG, Merckx T, et al. *Adv Energy Mater*. 2016;6(14):1600386.

80. Bi Z, Rodríguez-Martínez X, Aranda C, et al. Defect tolerant perovskite solar cells from blade coated non-toxic solvents. *J Mater Chem A*. 2018;6(39):19085-19093.

81. Huang YC, Li CF, Huang ZH, Liu PH, Tsao CS. Rapid and sheet-to-sheet slot-die coating manufacture of highly efficient perovskite solar cells processed under ambient air. *Sol Energy*. 2019;177:255-261.

82. Cai H, Liang X, Ye X, et al. High efficiency over 20% of perovskite solar cells by spray coating via a simple process. *ACS Appl Energy Mater*. 2020;3(10):9696-9702.

83. Mathies F, Eggers H, Richards BS, Hernandez-Sosa G, Lemmer U, Paetzold UW. Inkjet-printed triple cation perovskite solar cells. *ACS Appl Energy Mater*. 2018;1(5):1834-1839.

84. Vijayan A, Johansson MB, Svanström S, Cappel UB, Rensmo H, Boschloo G. Simple method for efficient slot-die coating of MAPbI$_3$ perovskite thin films in ambient air conditions. *ACS Appl Energy Mater*. 2020;3(5):4331-4337.

85. Bishop JE, Smith JA, Greenland C, et al. High-efficiency spray-coated perovskite solar cells utilizing vacuum-assisted solution processing. *ACS Appl Mater Interfaces*. 2018;10(46):39428-39434.

86. Whitaker JB, Kim DH, Larson BW, et al. Scalable slot-die coating of high performance perovskite solar cells. *Sustain Energy Fuels*. 2018;2(11):2442-2449.

87. Eggers H, Schackmar F, Abzieher T, et al. Inkjet-printed micrometer-thick perovskite solar cells with large columnar grains. *Adv Energy Mater*. 2020;10(6):1903184. https://doi.org/10.1002/aenm.201903184

88. Hwang K, Jung YS, Heo YJ, et al. Toward large scale roll-to-roll production of fully printed perovskite solar cells. *Adv Mater*. 2015;27(7):1241-1247.

89. Howard IA, Abzieher T, Hossain IM, et al. Coated and printed perovskites for photovoltaic applications. *Adv Mater*. 2019;31(26):1806702. https://doi.org/10.1002/adma.201806702

90. Xu F, Liu J, Subbiah AS, et al. Potassium thiocyanate-assisted enhancement of slot-die-coated perovskite films for high-performance solar cells. *Small Sci*. 2021;1(5):2000044. https://doi.org/10.1002/smsc.202000044

91. Gao LL, Li CX, Li CJ, Yang GJ. Large-area high-efficiency perovskite solar cells based on perovskite films dried by the multi-flow air knife method in air. *J Mater Chem A*. 2017;5(4):1548-1557.

92. Odabaşı Ç, Yıldırım R. Assessment of reproducibility, hysteresis, and stability relations in perovskite solar cells using machine learning. *Energ Technol*. 2020;8(12):1901449.

93. Vaynzof Y. The future of perovskite photovoltaics—thermal evaporation or solution processing? *Adv Energy Mater*. 2020;10(48): 2003073. https://doi.org/10.1002/aenm.202003073

94. Zhu X, Yang D, Yang R, et al. Superior stability for perovskite solar cells with 20% efficiency using vacuum co-evaporation. *Nanoscale*. 2017;9(34):12316-12323.

95. Ono LK, Leyden MR, Wang S, Qi Y. Organometal halide perovskite thin films and solar cells by vapor deposition. *J Mater Chem A*. 2016; 4(18):6693-6713.

96. Roß M, Gil-Escrig L, Al-Ashouri A, et al. Co-evaporated p-i-n perovskite solar cells beyond 20% efficiency: impact of substrate temperature and hole-transport layer. *ACS Appl Mater Interfaces*. 2020; 12(35):39261-39272.

97. Gil-Escrig L, Momblona C, La-Placa MG, Boix PP, Sessolo M, Bolink HJ. Vacuum deposited triple-cation mixed-halide perovskite solar cells. *Adv Energy Mater*. 2018;8(14):1703506. https://doi.org/10.1002/aenm.201703506

98. Saliba M, Matsui T, Seo JY, et al. Cesium-containing triple cation perovskite solar cells: improved stability, reproducibility and high efficiency. *Energ Environ Sci*. 2016;9(6):1989-1997.

99. Longo G, Momblona C, La-Placa MG, Gil-Escrig L, Sessolo M, Bolink HJ. Fully vacuum-processed wide band gap mixed-halide perovskite solar cells. *ACS Energy Lett*. 2018;3(1):214-219.

100. Yu Y, Zhao D, Grice CR, et al. Thermally evaporated methylammonium tin triiodide thin films for lead-free perovskite solar cell fabrication. *RSC Adv*. 2016;6(93):90248-90254.

101. Turan B, Huuskonen A, Kühn I, Kirchartz T, Haas S. Cost-effective absorber patterning of perovskite solar cells by nanosecond laser processing. *Sol RRL*. 2017;1(2):1700003.

102. Rakocevic L, Schöpe G, Turan B, et al. Perovskite modules with 99% geometrical fill factor using point contact interconnections design. *Prog Photovoltaics Res Appl*. 2020;28(11):1120-1127.

103. Rakocevic L, Gehlhaar R, Merckx T, et al. Interconnection optimization for highly efficient perovskite modules. *IEEE J Photovoltaics*. 2017;7(1):404-408.

104. Palma AL, Matteocci F, Agresti A, et al. Laser-patterning engineering for perovskite solar modules with 95% aperture ratio. *IEEE J Photovoltaics*. 2017;7(6):1674-1680.

105. Westin PO, Zimmermann U, Edoff M. Laser patterning of P2 interconnect via in thin-film CIGS PV modules. *Sol Energy Mater Sol Cells*. 2008;92(10):1230-1235.

106. Westin PO, Zimmermann U, Ruth M, Edoff M. Next generation interconnective laser patterning of CIGS thin film modules. *Sol Energy Mater Sol Cells*. 2011;95(4):1062-1068.

107. Gečys P, Markauskas E, Nishiwaki S, et al. CIGS thin-film solar module processing: case of high-speed laser scribing. *Sci Rep*. 2017;7(1): 1-9.

108. Cunningham D, Rubcich M, Skinner D. Cadmium telluride PV module manufacturing at BP Solar. *Prog Photovoltaics Res Appl*. 2002; 10(2):159-168.

109. Newport Corporation, Amorphous Silicon Thin Film Solar Cell Scribing. https://www.spectra-physics.com/mam/celum/celum_assets/resources/AppFocus_Si-Thin-Film-Solar-Scribing.pdf (accessed April 2021)

110. Lei T, Li F, Zhu X, et al. Flexible perovskite solar modules with functional layers fully vacuum deposited. *Sol RRL*. 2020;4(11):2000292.

111. Schultz C, Schneider F, Neubauer A, et al. Evidence of PbI$_2$-containing debris upon P2 nanosecond laser patterning of perovskite solar cells. *IEEE J Photovoltaics*. 2018;8(5):1244-1251.

112. Pisoni S, Fu F, Widmer R, et al. Impact of interlayer application on band bending for improved electron extraction for efficient flexible perovskite mini-modules. *Nano Energy*. 2018;49:300-307.

113. Walter A, Moon SJ, Kamino BA, et al. Closing the cell-to-module efficiency gap: a fully laser scribed perovskite minimodule with 16% steady-state aperture area efficiency. *IEEE J Photovoltaics*. 2018; 8(1):151-155.

114. Schultz C, Fenske M, Dagar J, et al. Ablation mechanisms of nanosecond and picosecond laser scribing for metal halide perovskite module interconnection—an experimental and numerical analysis. *Sol Energy*. 2020;198:410-418.

115. Turan B, Laser processing for the integrated series connection of thin-film silicon solar cells (No. RWTH-2016-01546). Lehrstuhl für Photovoltaik (FZ Jülich), 2015.

116. Stegemann B, Fink F, Endert H, et al. Novel concept for laser patterning of thin film solar cells. *Laser Tech J*. 2012;9(1):25-29.

117. Abzieher T, Feeney T, Schackmar F, et al. From groundwork to efficient solar cells: on the importance of the substrate material in co-evaporated perovskite solar cells. *Adv Funct Mater*. 2021;2104482. https://onlinelibrary.wiley.com/doi/full/10.1002/adfm.202104482

118. Rakocevic L, Gehlhaar R, Jaysankar M, et al. Translucent, color-neutral and efficient perovskite thin film solar modules. *J Mater Chem C*. 2018;6(12):3034-3041.

119. Ahmadian-Yazdi M-R, Eslamian M. Effect of Marangoni convection on the perovskite thin liquid film deposition. *Langmuir*. 2021;37(8): 2596-2606. https://doi.org/10.1021/acs.langmuir.0c03120

120. Schackmar F, Eggers H, Frericks M, et al. Perovskite solar cells with all-inkjet-printed absorber and charge transport layers. *Adv Mater Technol*. 2021;6(2):2000271. https://doi.org/10.1002/admt.202000271

121. Eisgruber IL, Sites JR. Extraction of individual-cell photocurrents and shunt resistances in encapsulated modules using large-scale laser scanning. *Prog Photovoltaics Res Appl*. 1996;4(1):63-75.

122. Bermudez V, Perez-Rodriguez A. Understanding the cell-to-module efficiency gap in Cu(In,Ga)(S,Se)$_2$ photovoltaics scale-up. *Nat Energy*. 2018;3(6):466-475.

123. Li J, Dewi HA, Wang H, et al. Co-evaporated MAPbI$_3$ with graded Fermi levels enables highly performing, scalable, and flexible p-i-n perovskite solar cells. *Adv Funct Mater*. 2021;2103252.

124. Borchert J, Milot RL, Patel JB, et al. Large-area, highly uniform evaporated formamidinium lead triiodide thin films for solar cells. *ACS Energy Lett*. 2017;2(12):2799-2804. https://doi.org/10.1021/acsenergylett.7b00967

125. Choi Y, Koo D, Jeong M, et al. Toward all-vacuum-processable perovskite solar cells with high efficiency, stability, and scalability enabled by fluorinated Spiro-OMeTAD through thermal evaporation. *Sol RRL*. 2021;5(9):2100415.

126. Booth H. Laser processing in industrial solar module manufacturing. *J Laser Micro/Nanoeng*. 2010;5(3):183-191.

SUPPORTING INFORMATION

Additional supporting information may be found in the online version of the article at the publisher's website.